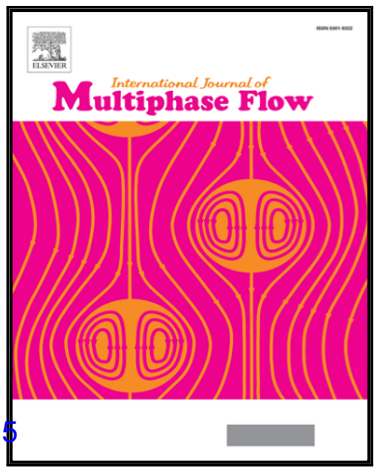

Numerical investigation of the aerodynamic breakup of droplets in tandem

Dionisis Stefanitsis , Ilias Malgarinos , George Strotos , Nikolaos Nikolopoulos , Emmanouil Kakaras , Manolis Gavaises

PII: S0301-9322(18)30245-3
DOI: https://doi.org/10.1016/j.ijmultiphaseflow.2018.10.015
Reference: IJMF 2909

To appear in: *International Journal of Multiphase Flow*

Received date: 3 April 2018
Revised date: 11 September 2018
Accepted date: 22 October 2018

Please cite this article as: Dionisis Stefanitsis , Ilias Malgarinos , George Strotos , Nikolaos Nikolopoulos , Emmanouil Kakaras , Manolis Gavaises , Numerical investigation of the aerodynamic breakup of droplets in tandem, *International Journal of Multiphase Flow* (2018), doi: https://doi.org/10.1016/j.ijmultiphaseflow.2018.10.015

Highlights

- Numerical examination of the aerodynamic breakup of four Diesel droplets in tandem formation at representative engine conditions.
- Identification of a new breakup mode in the multi-mode regime, termed as “shuttlecock”.
- Droplet proximity becomes important for non-dimensional distances between the droplets lower than 9.
- Drag coefficient and liquid surface area of the “representative chain droplet” are lower than the corresponding ones of the isolated droplet; breakup initiation time is longer and the critical *We* number is higher.
- Proposed correlations to predict the drag coefficient, liquid surface area, breakup initiation time and critical *We* of the “representative chain droplet”.

Numerical investigation of the aerodynamic breakup of droplets in tandem

Affiliations

Dionisis Stefanitsis[*1,2,] , Ilias Malgarinos[1,2], George Strotos[3], Nikolaos Nikolopoulos[1], Emmanouil Kakaras[1], Manolis Gavaises[2]

[1]Centre for Research and Technology Hellas/Chemical Process and Energy Resources Institute (CERTH/CPERI), Egialeias 52, Marousi, Greece

[2]City University London, School of Engineering and Mathematical Sciences, Northampton Square, EC1V 0HB London, UK

[3]Technological Educational Institute of Thessaly, Mechanical Engineering Department, 41110 Larissa, Greece

[*]Corresponding author: stefanitsis@certh.gr

malgarinos@lignite.gr, gstrot@teilar.gr, n.nikolopoulos@certh.gr, M.Gavaises@city.ac.uk, ekak@central.ntua.gr

Abstract

The present work examines the aerodynamic breakup of four liquid droplets in tandem formation at Diesel engine conditions using the Volume of Fluid (VOF) method. The examined Weber (*We*) numbers range from 15 up to 64 and the non-dimensional distances between the droplet centres (L/D_0) vary from 1.25 up to 20. Focus is given on the breakup process of the third droplet of the row, which is regarded as a "representative chain droplet"; its development is compared against that of an isolated droplet at the same flow conditions. It is found that for small distances and depending on the *We* number, the obtained shapes and breakup modes between the droplets are different, with the representative chain droplet experiencing a new breakup mode in the multi-mode regime, termed as "shuttlecock". This is characterized by an oblique peripheral stretching of the droplet caused by the acting of pressure forces at an off-centre region. Moreover, the drag coefficient and liquid surface area of the representative chain droplet are lower than the corresponding ones of the isolated droplet, while the breakup initiation time is longer and the minimum *We* number required for breakup (critical *We*) is higher; correlations are provided to quantify the effect of droplet distance on the aforementioned quantities. Generally, the droplet proximity becomes important for L/D_0<9. Finally, the predicted drag coefficient is utilised in a simplified 0-D model that is capable of estimating the temporal evolution of droplet velocity of the representative chain droplet.

Keywords

Chain droplet breakup; Diesel; drag coefficient; breakup time; critical *We*.

Nomenclature

Roman symbols

A	Area [m^2]
B	Average dimensionless deformation rate [-]
C_d	Drag coefficient [-]
CF	Correction factor [-]

Greek symbols

ε	Density ratio [-]
μ	Dynamic viscosity [kg/(m·s)]
ρ	Density [kg/m^3]
σ	Surface tension [N/m]

D	Droplet diameter [m]	φ	General droplet quantity
L	Distance between droplet centres [m]	**Subscripts**	
N	Viscosity ratio [-]	0	Initial
Oh	Ohnesorge number [-]	cr	Critical
P	Pressure [Pa]	$cross$	Cross-stream
Re	Reynolds number [-]	d	Droplet
S	Droplet surface area [m^2]	f	Frontal
T	Temperature [K]	g	Gas phase
t	Time [s]	is	Isolated droplet
t^*	Non-dimensional time [-]	L	Liquid phase
t_{br}	Breakup initiation time [s]	max	Maximum
t_{sh}	Shear breakup timescale [s]	RCD	Representative chain droplet
U	Velocity [m/s]	rel	Relative
We	Weber number [-]	str	Streamwise

1 Introduction

Droplet deformation and breakup occur in a wide variety of systems and applications from mass spectrometry to internal combustion engines [1]. The non-dimensional numbers that describe the breakup of isolated droplets, i.e. droplets that are not influenced by the presence of other ones in their proximity, are the Weber (We), Ohnesorge (Oh) and Reynolds (Re) numbers as well as the density (ε) and viscosity ratios (N) of the two phases [2]; nevertheless, only four of them are required to fully describe the phenomenon since the fifth number can be expressed as a combination of the rest.

$$We = \frac{\rho_g U_{rel,0}^2 D_0}{\sigma} \qquad Oh = \frac{\mu_L}{\sqrt{\rho_L \sigma D_0}} \qquad Re = \frac{\rho_g U_{rel,0} D_0}{\mu_g} \qquad \varepsilon = \frac{\rho_L}{\rho_g} \qquad N = \frac{\mu_L}{\mu_g} \tag{1}$$

The breakup timescale proposed by Nicholls and Ranger [3] can be used as a convenient non-dimensionalisation parameter for time:

$$t_{sh} = \frac{D_0}{U_{rel,0}} \sqrt{\varepsilon} \tag{2}$$

Although the aerodynamic breakup of isolated droplets has been thoroughly investigated (see for example [2] among many others), not much attention has been given to the breakup of a droplet cluster, in which there is interaction between the droplets; such cases are more representative for sprays having droplets in close proximity. For example, a typical Diesel spray consists of ~10^7 droplets, occupying a volume of ~250mm^3 [1]; assuming an average droplet size of 10μm [1, 4], the average distance between the droplets (L/D_0) can be estimated to be around 2.5 but obviously this number will take smaller values closer to the injector nozzle.

The aerodynamic and hydrodynamic interaction between rigid bodies has been initially studied with respect to the collective motion of animals, such as flocks of birds, schools of fish and swarms of insects. Earlier theoretical works on the flight formation of birds [5-8] focused on the examination of

the so called V formation and showed that it is more energetically efficient due to lower drag and higher lift, compared to the isolated flying of birds. Later, numerical studies [9-11] verified these results by performing CFD simulations with artificial birds (plates or cylinders) and also studied the effect of various parameters such as the angle of the V formation, the number of birds and their distance. They found that the energy efficiency is higher at larger numbers of birds and lower distances, while the formation becomes more stable at larger angles. Moreover, CFD simulations with schools of fish [12-20] indicate that swimming in schools is more advantageous than isolated swimming in terms of energy efficiency due to lower drag and sideways forces; this was attributed mainly to the exploitation of the reverse von Karman vortex streets by the downstream fishes. Finally, it was found that triangular and rectangular formations are more efficient than tandem ones, indicating that a diamond-like configuration is the most efficient hydrodynamically for the swimming of schools of fish.

Turning now to the the examination of the interaction between liquid droplets, the majority of the previous studies is focused on deforming (but without breakup) droplets, characterized by low *Re* and *We* numbers. Liu et al. [21] studied the deformation of monodisperse droplets both experimentally and numerically (using periodic boundary conditions) for *Re* numbers ranging from 20 up to 100 and non-dimensional distances between the droplets from 2 to 12. Their study was focused on the investigation of the drag coefficient and found that the drag coefficient of droplets in an infinite chain is up to an order of magnitude smaller than the drag coefficient of a single isolated droplet for L/D_0=2. Mulholland et al. [22] studied the drag coefficient of droplets in a monodispersed stream for *Re* numbers ranging from 90 to 290 and L/D_0 from 1.7 to 1700. Based on the results of the study, an empirical model for the computation of the drag coefficient was proposed, which was able to predict the droplet trajectories with acceptable accuracy. Temkin and Ecker [23] investigated experimentally the binary interaction of water droplets exposed in the flow behind a weak shock wave for *Re* numbers lower than 150, horizontal distance between the droplets from 1.5 up to 11 and vertical one from 3 to 6. They concluded that the leading droplet is not affected by the trailing in terms of drag force, while the latter experiences reduction in its drag coefficient up to 50% relative to its isolated value. Poo and Ashgriz [24] also investigated the variation of the drag coefficient in a droplet stream present in a turbulent flow and found a decrease in the drag coefficient by a factor of 4 to 5 compared to the drag coefficient of a solid sphere at the same conditions. Nguyen and Dunn-Rankin [25] conducted experiments with droplet packets (1-6 droplets) travelling vertically in an air stream for *Re*=80 and L/D_0=5.2, and found that the average drag of the trailing droplet was 25% lower than that of the leading one. From the same research group, Connon and Dunn-Rankin [26] studied the behaviour of a droplet flowing parallel to an infinite droplet stream and their main outcome was that the isolated droplet is influenced for values of L/D_0 lower than 15. Hollander and Zaripov [27] performed experiments with a monodisperse droplet stream for *Re* numbers ranging from 1 up to 10 and proposed a correction for the drag coefficient in the droplet momentum equation, so that the presence of other droplets, can be taken into consideration.

Regarding the numerical modelling of droplet chains, Kim et al. [28-30] studied the flow over two solid and liquid spheres using a three-dimensional implicit finite-difference algorithm for *Re* numbers ranging from 50 up to 150 and non-dimensional distances from 1.5 up to 25. They examined the flow structure and drag coefficient, and observed that the latter becomes almost identical to that of the isolated droplet for L/D_0 >9. Prahl et al. [31] performed 3D simulations using the VOF method of

single and dual droplets in a uniform flow with *Re*=100 and *We*=0.1 and 1. The non-dimensional distance between droplets varied from 1.5 up to 6 and the drag coefficient was calculated for the downstream droplet compared to the leading, as well as the isolated ones. Later studies examined higher *We* and *Re* numbers resulting in highly deforming droplets. In this respect, Quan et al. [32, 33] used a moving mesh interface tracking scheme coupled with the finite volume method to study the dynamics of two deformable droplets placed in tandem and subjected to a sudden acceleration by a gaseous flow. The examined *We* numbers ranged from 0.4 up to 40, the *Oh* number from 0.1 up to 1.1, the *Re* number was equal to 40, the non-dimensional distances between the droplets ranged from 1.3 up to 6 and the density and viscosity ratios of the two phases were both equal to 50 (*Oh*=0.1-1.1). They observed that the two droplets form a mushroom shape during their deformation and also that the drag coefficient of the trailing droplet is greatly reduced, while that of the leading is less affected, compared to that of the isolated droplet. Finally, Magi and Abraham [34] used a lattice-Boltzmann method to simulate binary and ternary systems of drops moving in tandem formation into a quiescent gas. The examined density and viscosity ratios were equal to 5, the *Oh* number equal to 0.025, the *We* number equal to 20 and 50 and the L/D_0 equal to 1.5. Their main conclusions were that for the case of ternary droplets the two trailing droplets decelerate slower than the isolated one, while the leading droplet breaks up faster followed by the middle one. Summarizing, all studies (experimental and numerical) on the effect of the distance between particles/droplets have shown that the trailing particle/droplet exhibits a reduction in the drag coefficient relative to the trailing one.

To the authors' best knowledge, the current study is the first one that investigates numerically the aerodynamic breakup of four Diesel droplets arranged in tandem formation for a wider range of *We* and L/D_0 numbers than those examined so far. The examined *We* and L/D_0 of the current study are depicted in Figure 1 along with those of the previous numerical studies. The purpose of the study is to provide a breakup map in the L/D_0–*We* plane, and correlations for the prediction of a) the maximum liquid surface area, b) the breakup initiation time and c) the drag coefficient, as functions of *We* and L/D_0, of the third droplet of the row, which is considered as "representative chain droplet", RCD, (see Appendix A). The proposed correlations can be used in CFD codes employed for the simulation of sprays, as they provide a better estimation of the aforementioned quantities compared to the correlations derived for isolated droplets. Nevertheless, in realistic spray conditions droplets are influenced by the presence of other droplets in the direction parallel to the flow, which affect their deformation and breakup characteristics [1]; however, such effects are not examined in the current work.

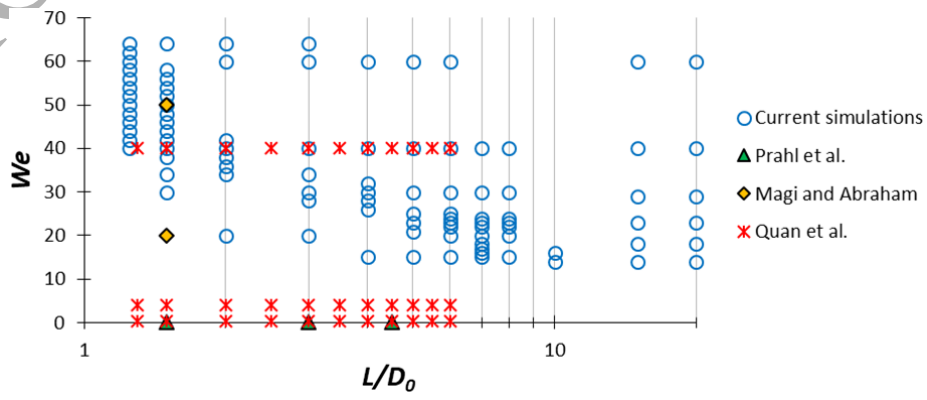

Figure 1. Examined *We* and L/D_0 numbers in the current and previous numerical studies.

The paper is organized as follows: first, the computational setup and examined conditions are described, followed by a section about the temporal evolution of droplet shapes and their comparison for the leading, the representative chain and the isolated droplets. Subsequently, the numerical results for the quantities of the critical *We* number, the maximum droplet surface area, the breakup initiation time and the drag coefficient of the representative chain droplet are presented and correlations are proposed for their prediction as functions of *We* and L/D_0 (summarized in Table 2 at the end of the paper). Finally, the overall assessment of the effect of L/D_0 on the representative chain droplet is presented, and the main conclusions are summarized in the last section of the paper.

2 Computational setup and examined conditions

The flow present in the aerodynamic breakup of droplets is considered as incompressible and laminar, mathematically described by the Navier-Stokes equations, the continuity equation and the Volume of Fluid (VOF) equation of [35] for tracking the interface between the liquid droplets and the surrounding gas. In order to model the surface tension forces in the momentum equation the Continuum Surface Stress (CSS) model of [36] is utilized. Two-dimensional axisymmetric simulations are performed with the commercial CFD tool ANSYS FLUENT v16 [37]. The finite volume method (FVM) [38] is applied for the formulation of the equations, while the resulting system is solved with the PISO algorithm [39] of the segregated pressure-based solver [40]. The pressure equation is spatially discretized using the body force weighted scheme [40], while for the momentum equation the second order upwind scheme [41] is utilized. The VOF equation is solved implicitly and is spatially discretized with the compressive scheme [40]. The temporal discretization of all equations is done with the bounded second order implicit scheme [40]. In addition, various User Defined Functions (UDFs) are utilized for i) the adaptive local grid refinement technique around the liquid-gas interface [42], ii) the adaptive time-step scheme for the implicit VOF solver based on the velocity at the droplet interface [43], and iii) the moving mesh technique based on the average velocity of the droplets. The CFD model has been developed and validated in previous works for a number of applications, among else the free fall of droplet [42], the droplet impingement on a flat wall [44] or a spherical particle [45-47], the aerodynamic droplet breakup [43, 48-52] and the droplet evaporation [43, 50, 53].

The 2-dimensional axisymmetric computational domain and boundary conditions are shown in Figure 2. The four droplets are placed in tandem formation moving with an initial velocity $U_{d,0}$ in stagnant air (boundary condition for velocity inlet $U=0$). A 3-D simulation would require approximately a thousand times more computational resources (CPU·hours) compared to a 2-D one; for this reason, the 2-D axisymmetric approach is employed in the current study instead of the 3-D one. Apart from the three-dimensional nature of droplet breakup, which becomes important at the last stages of breakup, limitations of axisymmetric simulations appear in the deformation and breakup of droplets due to turbulence and vortex shedding [54]. Nevertheless, at low Reynolds numbers the axisymmetric approximation has proven to be relatively accurate during deformation stages [51, 55, 56]. In addition, in [57, 58] some 3D simulations show that symmetry is present in the low Reynolds regime. Finally, the axisymmetric simulations do not allow the prediction of the characteristics of the secondary droplets resulting from the breakup of the main droplet, which is not the aim of the current work.

The grid comprises of rectangular cells with a base grid resolution equal to 3cpR (cells per radius) followed by the implementation of 6 levels of local grid refinement, to obtain the desired resolution of 192cpR around the liquid-gas interface. The refinement algorithm is solely based on the interface location and is presented in detail in [44]. Systematic runs with 96, 192 and 384cpR have shown that the resolution of 192cpR is adequate for the simulations of droplets in tandem since the average velocity and deformation of the RCD change less than 2% when a finer grid is used.

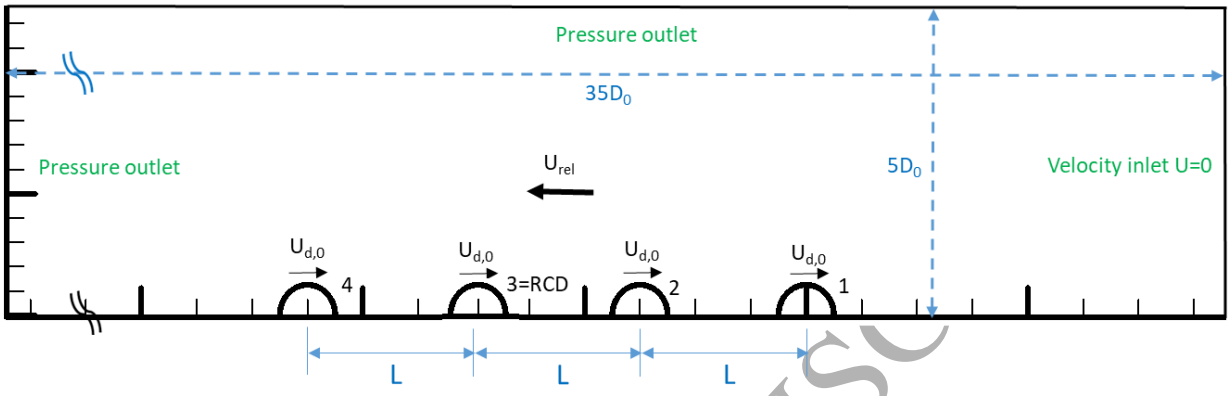

Figure 2. Computational domain and boundary conditions for a case with L/D_0=2.

The droplet diameter and the conditions of the surrounding air correspond to those of Diesel engines as presented in Table 1, along with the corresponding references used for their estimation. It should be noted that at such high air temperature, evaporation of the droplets takes places, which is neglected in the current work; focus here is given to the aerodynamic deformation and breakup. The resulting non-dimensional numbers from these conditions are: Oh=0.05, ε=51 and N=37. By changing the initial droplet velocity, the obtained We numbers range from 15 up to 64, while the Re number lies in the range of 402 to 860; it is to be noted that these conditions correspond to bag and multi-mode breakup for isolated droplets. The examined non-dimensional distances measured from the droplet centres (L/D_0) range from 1.25 up to 20, resulting in 96 examined cases in total (see Figure 1). Finally, simulations have been performed also for an isolated droplet using the same computational domain and conditions in order to compare the results (11 simulations in total in the range of We=15-64).

Table 1. Representative Diesel engine conditions.

	D_0 (μm)	P (bar)	T_g (K)	μ_g(kg/s·m)	ρ_g (kg/m^3)	T_L (K)	μ_L(kg/m·s)	ρ_L(kg/m^3)	σ (N/m)
Value	50	40	900	4E-05	15.48	335	0.0015	788.6	0.024
Reference	[4]	[59]	[59]	[60]	Ideal gas law	[59]	[61]	[61]	[62]

The different quantities of the representative chain droplet (maximum surface area, breakup initiation time and drag coefficient) can be calculated as a product of two terms: i) the value of the corresponding quantity of an isolated droplet at the same conditions (Appendix B), and ii) a correction factor that accounts for the interaction between the droplets. The correction factor is a function of We and L/D_0 and is given in its general form in equation (3). The symbol φ denotes the respective examined quantity (S_{max}/S_0, t_{br}, C_d) and the subscripts "*is*" and "*RCD*" stand for the isolated and representative chain droplets, respectively. The plus sign is used for the quantities that are

higher compared to the corresponding values of an isolated droplet (such as t_{br}), while the minus one for those that are lower (such as S_{max}/S_0 and C_d). When the *We* and L/D_0 are large enough, the correction factor approaches unity, i.e. the two droplets have a similar behavior. Conversely, when the *We* and L/D_0 are small enough the correction factor approaches zero, i.e. the representative chain droplet is totally covered by its upstream droplet. The equation for the drag reduction due to L/D_0 is in agreement with the correlation proposed by [27], in which the ratio $C_{d,RCD}/C_{d,is}$ decreases with the inverse exponential of L/D_0.

$$CF_{\varphi} = \frac{\varphi_{RCD}}{\varphi_{is}} = 1 \pm e^{-f\left(We,\frac{L}{D_0}\right)} \quad (3)$$

With

$$f\left(We,\frac{L}{D_0}\right) = c_1 \cdot We^{c_2} \cdot \left(\frac{L}{D_0} - 1\right)^{c_3} \quad (3b)$$

The coefficients c_1, c_2 and c_3 appearing in equation (3), as well as those of the isolated droplet are found by fitting to the results of the simulations for the corresponding quantity, and are summarized in Table 2 of section 3.6.

3 Results and discussion

3.1 Droplet shapes

In Figure 3, the temporal evolution of the droplets' shape (denoted with the VOF iso-value of 0.5) is presented at different time instances for a representative case of droplet chain (*We*=40, L/D_0=2) along with the one of an isolated droplet at the same *We* number. The first observation is that the leading and isolated droplets exhibit a quite similar evolution of droplet shape and experience the same breakup mode (multi-bag), something that holds true for all the examined cases, as expected. Nevertheless, despite the similarity in droplet shapes, for small L/D_0 the drag coefficient of the leading droplet decreases up to 30% compared to the corresponding value of the isolated droplet, while the breakup initiation time and maximum surface area are slightly lower.

On the other hand, the shapes of the trailing droplets (no. 2, 3 and 4) after t/t_{sh}=1.0 start to deviate from those of the isolated droplet, as they are influenced by the presence of their upstream droplets (Appendix C presents a quantitative comparison between droplets 1, 2, 3 and 4). More specifically, their shapes are more deformed in the streamwise direction, which is due to the faster air flow observed at their periphery compared to their centre (in terms of relative velocity), as indicated by the streamlines of Figure 3. In addition, they also encounter higher pressure at their periphery rather than their centre (again after t/t_{sh}=1.0), as shown in Figure 4, where the contour of dimensionless pressure ($= (P - P_{\infty})/\frac{1}{2}\rho_g U_{d,0}^2$) is presented for the same conditions (*We*=40, L/D_0=2). As a result, an oblique pressure gradient is developing, which tends to stretch the droplet towards a 45deg downstream direction; this alters their breakup mode in relevance to the one of the isolated droplet (multi-bag). This breakup mode has not been reported so far in the literature and it is termed here as "shuttlecock", as its shape resembles that of a shuttlecock ball used in Badminton. This was observed for *We* numbers in the range of 16 to 64 and droplet distances ranging from 1.25 to 4 (see Figure 7 of

section 3.2). When the distance between the droplets becomes large enough (L/D_0>5 for We=40) their shapes and breakup modes become similar to those of the isolated droplet (multi-bag), as it is shown in Figure 5. In addition, the trailing droplets move faster than the leading one (due to lower drag) and therefore get closer to it (especially evident for the first two droplets), which might result in their collision at subsequent time instances.

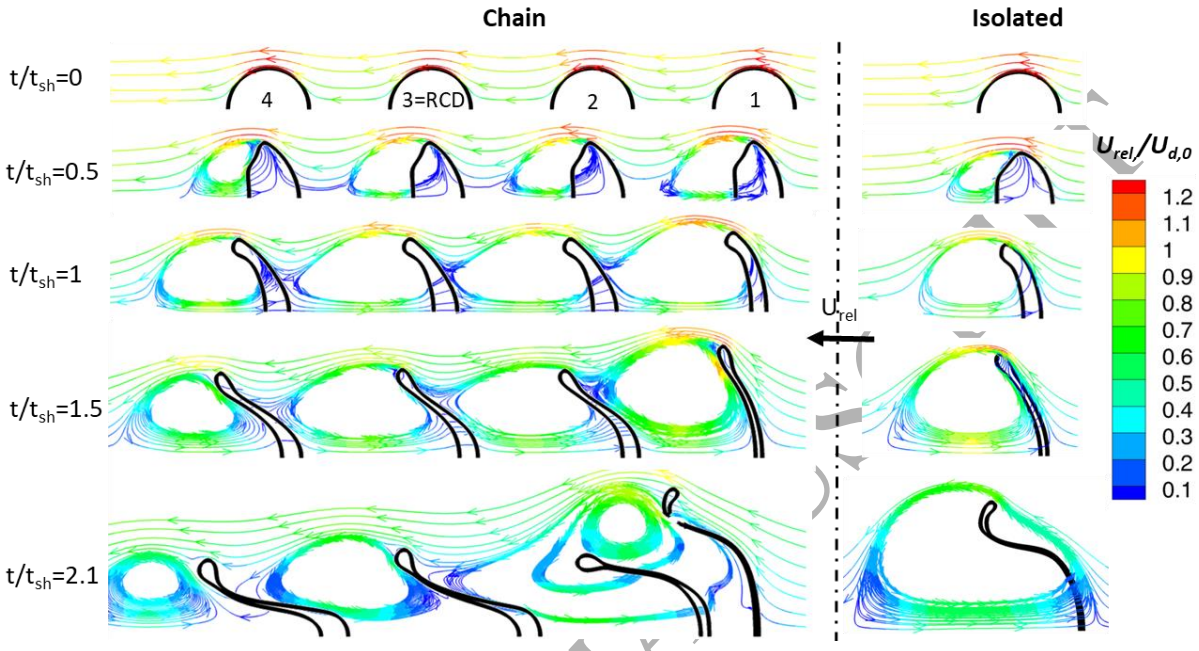

Figure 3. Temporal evolution of droplet shape for chain (We=40, L/D_0=2) and isolated (We=40) droplets (streamlines colored with the non-dimensional relative velocity magnitude).

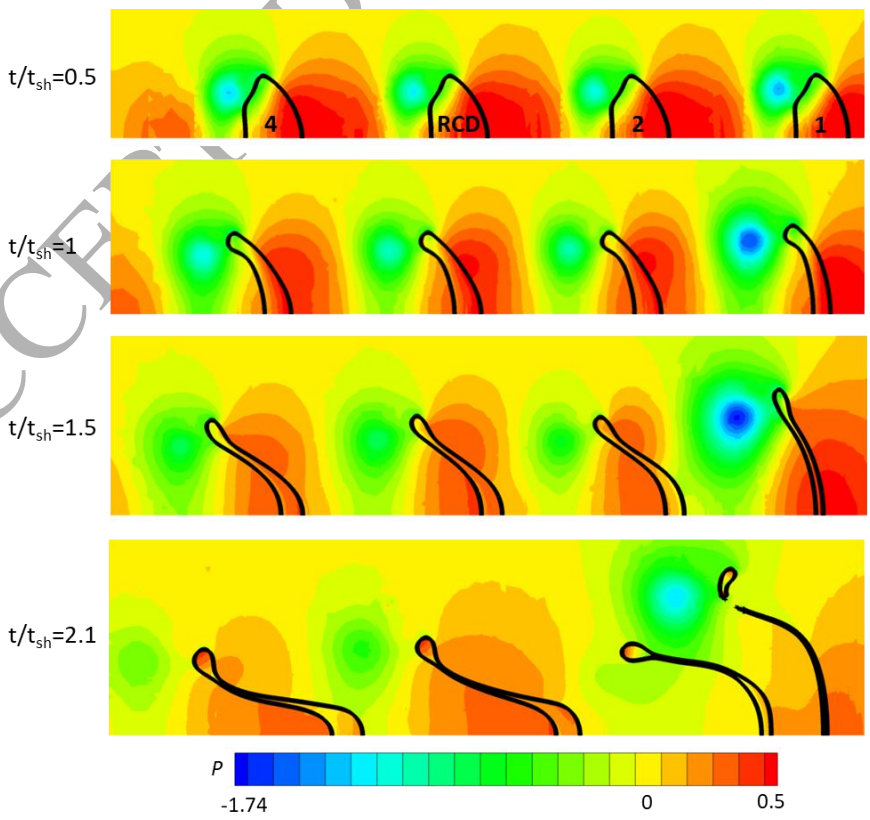

Figure 4. Dimensionless pressure contour for *We*=40 and L/D_0=2.

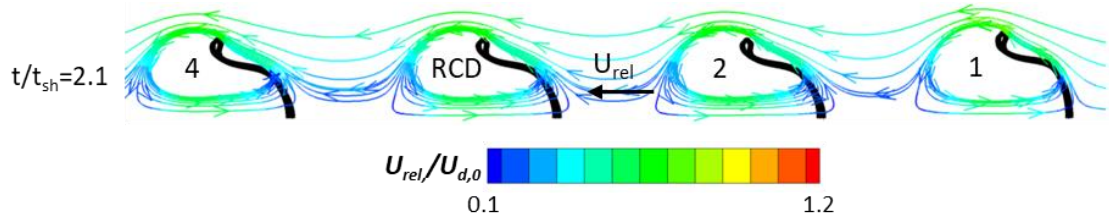

Figure 5. Snapshot of droplet shapes for *We*=40 and L/D_0=5.

For the same distance between the droplets (L/D_0=2), Figure 6 presents the temporal evolution of droplet shape of the representative chain and the isolated droplets for two *We* numbers (20 and 60). It is observed that for the low *We* of 20 the representative chain droplet deforms up to a maximum point and then reaches an elongated spheroid shape without breaking (Figure 6a). This elongated spheroid shape differs from the spherical shape reported in the literature for low *We* (oscillatory deformation) [2], since it is affected by the presence of the upstream droplet, which hinders the incoming air flow. For the same *We* number the isolated droplet experiences bag breakup mode. On the other hand, when the *We* number increases to 60, both the representative chain and the isolated droplets experience multi-bag breakup mode, as shown in Figure 6b, indicating that for high *We* numbers the effect of distance between the droplets is minimized and thus their deformation rates and shapes become independent.

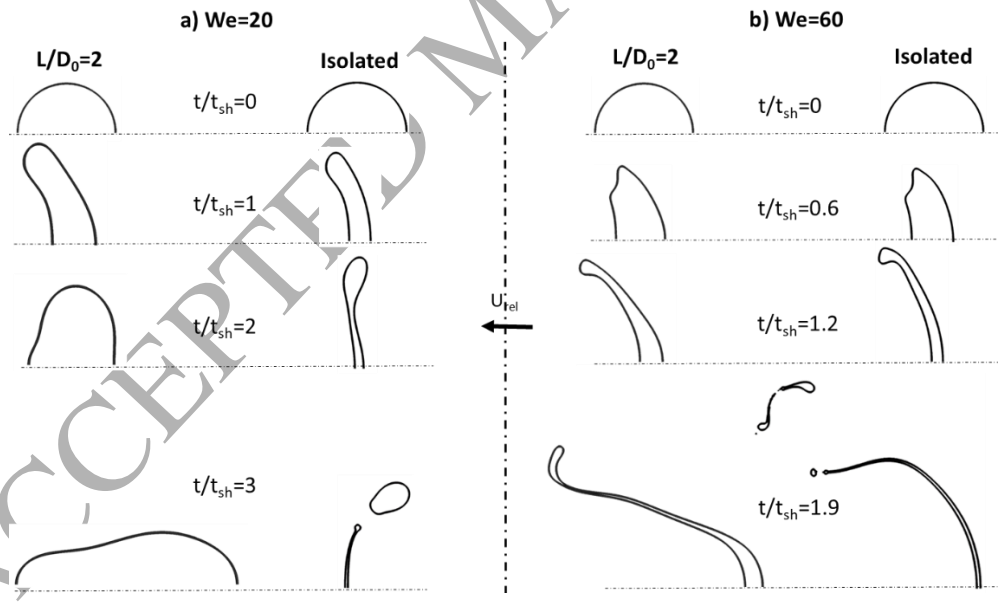

Figure 6. Temporal evolution of droplet shape for chain (L/D_0=2) and isolated droplets with a) *We*=20 and b) *We*=60.

3.2 Breakup map

Figure 7 presents the simulated cases of the current work in the L/D_0-*We* map: the blue circles correspond to the cases that the representative chain droplet deforms without breaking up (Figure 6a), the red triangles to the cases that the droplets are clearly breaking up (Figure 6b), and finally the yellow diamonds correspond to the cases that the droplets become very thin without breaking

(Figure 3 for t/t_{sh}=2.1). For the latter case it is quite likely that a 3D simulation would predict breakup and therefore in the current work they are considered as transition points between breakup and no-breakup. It is apparent from Figure 7 that as the droplet distance L/D_0 decreases, the minimum *We* number required for the breakup to occur (critical *We*) is increasing. The critical *We* number as a function of L/D_0 can be estimated using equation (4), similar to eq. (3), and is presented in Figure 7. It is observed that for large L/D_0 the value of the critical *We* number approaches the value of the isolated droplet, which is found equal to 14 from the simulation of an isolated droplet at the same conditions (*Oh*, *Re*, ε). In general the critical *We* number of an isolated droplet depends on the flow conditions and in [63] a correlation is proposed that can predict it, as a function of the non-dimensional numbers *Oh*, *Re* and ε. For small L/D_0 the We_{cr} increases rapidly as the representative chain droplet is greatly influenced by the upstream one.

$$CF_{We_{cr}} = \frac{We_{cr,RCD}}{We_{cr,is}} = 1 + c_1 \cdot \left(\frac{L}{D_0}\right)^{-c_2} \quad (4)$$

with c_1=5.5 and c_2=2.2.

In addition, Figure 7 presents the regions of the different breakup regimes encountered in the simulations (bag, shuttlecock and multi-bag). The bag breakup regime is encountered at *We* numbers in the range of 15 to 25 and droplet distances L/D_0 higher than 4, the multi-bag regime from *We*=26 up to 64 and for L/D_0 higher than 1.5, and the shuttlecock regime from *We*=16 up to 64 and L/D_0 less than 5.

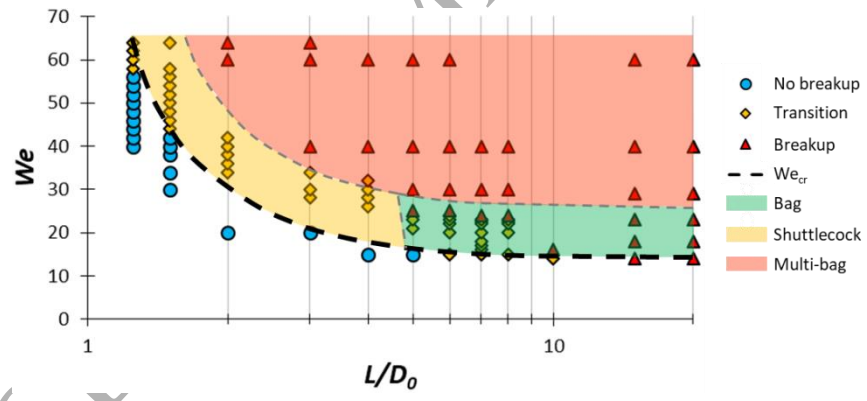

Figure 7. L/D_0-*We* map with the simulated cases along with the regions of the various breakup regimes (*Oh*=0.05, ε=51 and *N*=37).

3.3 Droplet surface area

One quantity that is important for spray applications and is difficult to be measured experimentally is the surface area of the droplet, which is calculated from the CFD data as $S = \sum_i^{ncells} V_{cell}|\nabla a|$. The current work is dealing with the maximum surface area of the droplet corresponding to either the surface area at the instance of breakup or the maximum surface area for the droplets undergoing deformation. The ratio of the maximum surface area of the representative chain to the isolated droplet $S_{max,RCD}/S_{max,is}$ is presented in Figure 8 as a function of *We* and L/D_0. The colored dots correspond to the results of the CFD simulations, while the iso-lines (0.3, 0.6, 0.9 and 0.99) to the predictions of the proposed equation (3), with c_1=0.21, c_2=0.35 and c_3=0.79. For instance, the iso-line

0.6 corresponds to a 40% reduction in maximum surface area, relative to the one of an isolated droplet. It is observed that as the L/D_0 decreases, the ratio $S_{max,RCD}/S_{max,is}$ also decreases since the representative chain droplet is affected by the wake of its upstream droplet, reaching values as low as 0.21, indicating a strong influence of the maximum surface area on the droplet distance. Conversely, as the L/D_0 increases, the ratio $S_{max,RCD}/S_{max,is}$ approaches unity and the maximum liquid surface area of the representative chain droplet approaches the corresponding value of the isolated one. Finally, the dependence of the ratio on the *We* number is weak, as indicated by the almost vertical iso-lines.

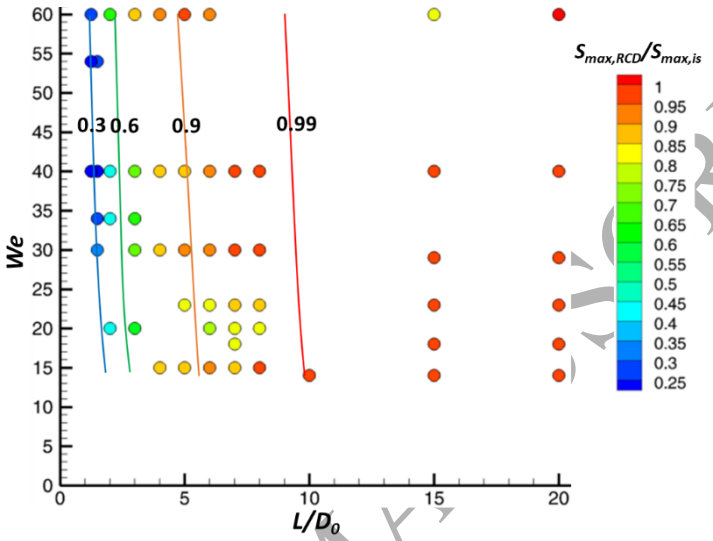

Figure 8. Ratio $S_{max,RCD}/S_{max,is}$ as function of *We* and L/D_0 (scatter: CFD, lines: equation (3)).

3.4 Breakup initiation time

Similar to the droplet surface area, the breakup initiation time of the representative chain droplet is also different from that of the isolated one for the same conditions. By looking back at Figure 3 for t/t_{sh}=2.1, we observe that the trailing droplets break up later than the isolated one. Figure 9 presents the ratio $t_{br,RCD}/t_{br,is}$ as a function of *We* and L/D_0, as predicted by the CFD simulations (colored dots) and equation (3) (iso-lines), with c_1=0.1, c_2=0.64 and c_3= 0.71; only the cases that actually break up are taken into account, i.e. the red triangles of Figure 7. We notice that for large L/D_0 the ratio $t_{br,RCD}/t_{br,is}$ approaches unity (similar to $S_{max,RCD}/S_{max,is}$), while as the L/D_0 decreases the breakup time of the representative droplet increases. The effect of L/D_0 on this ratio is larger at lower *We* numbers, while for the examined cases the breakup time is not increasing more than 23% compared to that of an isolated droplet.

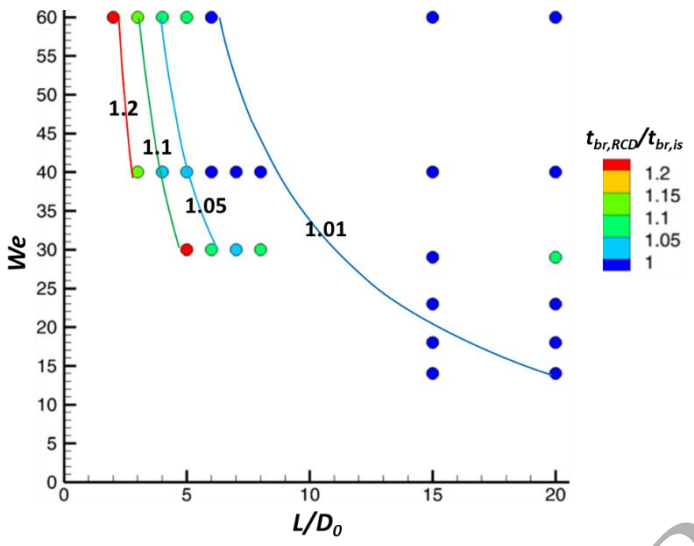

Figure 9. Ratio $t_{br,RCD}/t_{br,is}$ as function of *We* and L/D_0 (scatter: CFD, lines: equation (3)).

3.5 Drag coefficient

The drag coefficient of a deforming droplet is also an important quantity used in macroscopic CFD spray codes, especially those following the Lagrangian approach. The drag coefficient can be found from the droplet force balance in the streamwise direction [64], which is given for a decelerating droplet in equation (5) (particle motion equation). The terms representing the effect of the gravity, virtual mass, pressure and stress forces have been neglected (since ρ_g/ρ_L<<1) [40], while the effect of Basset force has been incorporated into the drag coefficient (pertaining to an effective drag coefficient), similar to previous numerical studies [65-68]. The droplet velocity is the volumetric averaged one.

$$\frac{dU_d(t)}{dt} = -C_d(t) \cdot \frac{A_f(t)}{A_{f,0}} \cdot \frac{3}{4D_0\varepsilon} \cdot {U_d}^2 \tag{5}$$

As seen from equation (5), an estimation of the droplet frontal area variation ($A_f(t)/A_{f,0}$) is needed in order to calculate the drag coefficient of a deforming droplet. Pilch and Erdman [69] excluded the frontal area term from equation (5) and its effect was incorporated into the drag coefficient. This method was later utilized by [43] and [68] for the calculation of the average drag coefficient of a deforming droplet as function of the *Re* number, and is also presented in the current work in Appendix D. Another method, proposed initially by [70, 71] and utilized later by [40, 72], assumes that the drag coefficient of a deforming droplet can be estimated as a linear interpolation between the drag coefficient of a spherical object (initial droplet shape) and that of disk (deformed droplet shape) for the same *Re* number, depending on the droplet deformation. This geometrical estimation of the drag coefficient requires the solution of an additional equation for the prediction of droplet deformation as a function of time, which might be computationally costly when applied to macroscopic spray models for a very large number of droplets. In this work we propose a method in which the droplet frontal area is assumed to vary linearly with time (equation (6), where $t^*=t/t_{sh}$), in an attempt to simplify as much as possible the calculations. This is a first step towards the estimation of the temporal variation of droplet frontal area, whereas more accurate and complex models can be later utilized such as those used in macroscopic CFD codes for the prediction of the temporal

variation of droplet deformation. Such models are the Taylor Analogy Breakup (TAB) model [73], the Droplet Breakup and Deformation (DBB) model [74] and the Clark's model [75] among others. The linear approach followed in the current study applies only to droplets experiencing breakup and therefore is utilized only for the cases corresponding to the breakup and transition points of Figure 7.

$$\frac{A_f(t^*)}{A_{f,0}} = 1 + B \cdot t^* \tag{6}$$

The factor *B* represents the average dimensionless deformation rate given by equation (7), where t^*_{max} is the time instance corresponding to $S=S_{max}$ up to which the drag coefficient is calculated. This time instance is chosen instead of the actual breakup time because in some cases droplets do not clearly break (transition points in Figure 7).

$$B = \frac{\frac{A_f(t^*_{max})}{A_{f,0}} - 1}{t^*_{max}} \tag{7}$$

By substituting equations (6) and (7) into equation (5) and integrating for t^* we get equation (8), which gives the temporal evolution of droplet velocity; note that an average drag coefficient $\overline{C_d}$ is used instead of $C_d(t)$. By fitting equation (8) to the results of the simulations ($U_d - t^*$) the average drag coefficient of each case is calculated.

$$U_d(t^*) = \frac{U_{d,0}}{\overline{C_d} \cdot \frac{3}{4\sqrt{\varepsilon}} \cdot (t^* + \frac{B \cdot (t^*)^2}{2}) + 1} \tag{8}$$

The results of the ratio $\overline{C_{d,RCD}}/\overline{C_{d,ls}}$ are shown in Figure 10 as a function of *We* and L/D_0 as calculated by the CFD simulations (colored circles) along with the predictions of equation (3) (iso-lines), with c_1= 0.038, c_2= 1.1 and c_3= 0.53. The ratio $\overline{C_{d,RCD}}/\overline{C_{d,ls}}$ decreases when the ratio L/D_0 is decreasing, in agreement with previous studies [28-33], reaching values down to 0.75. A strong dependence of the ratio on the *We* number is observed as depicted by the iso-lines, something that is attributed to the dependence of the frontal area on the *We* number as well.

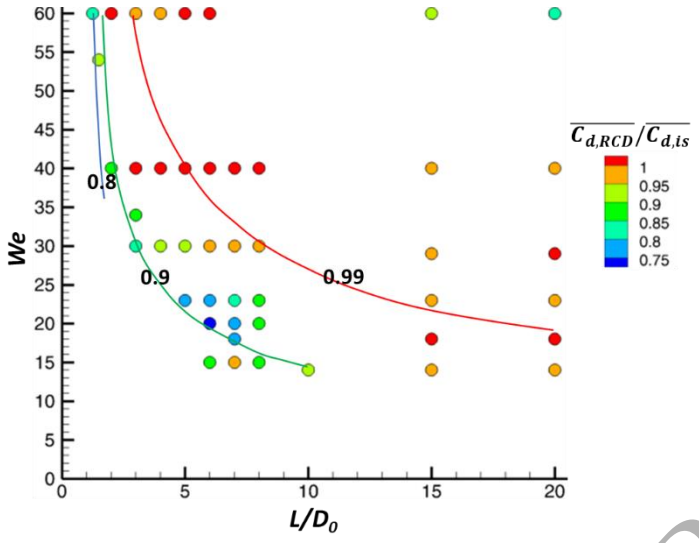

Figure 10. Ratio $\overline{C_{d,RCD}}/\overline{C_{d,ts}}$ as function of *We* and L/D_0 (scatter: CFD, lines: equation (3)).

Finally, equation (8) predicts the temporal evolution of droplet velocity, using C_d and B from equation (3). Figure 11 presents the temporal evolution of droplet velocity of a representative chain droplet for two *We* numbers (40 and 60) and L/D_0=2 as predicted by the equation and the CFD simulations, up to the point of breakup initiation. As it is observed from the figure there is a good agreement between the simulations and the predictions from the equation for both *We* numbers up to approximately t/t_{sh}=1.6, while after that point a deviation is observed. The velocity as predicted by the CFD simulations seems to approach a constant value, while that of the equation continues to decrease. This observed trend in the simulations is due to the low air velocity (in terms of the relative one) appearing in the upstream of the representative chain droplet, which is attributed to the wake induced by the upstream droplet (see Figure 3 of chapter 3.1 for t/t_{sh}=2.1). For the cases characterized by larger L/D_0, the results resemble those of an isolated droplet at the same conditions (see Figure 15 in Appendix B).

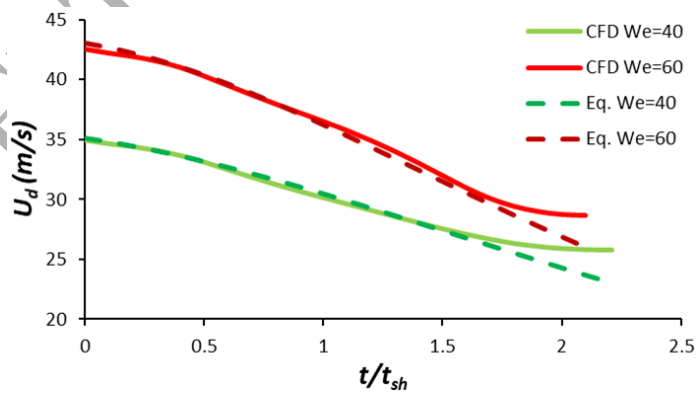

Figure 11. Temporal evolution of droplet velocity for two *We* numbers (40 and 60) and L/D_0=2 as predicted by the CFD simulations and the correlation (8).

3.6 Overall assessment of the effect of droplet distance L/D_0

In order to summarize the effect of the droplet distance L/D_0 on the deformation of a representative chain droplet, a marked area is identified in the map L/D_0-*We*, where the effect of L/D_0 can be

considered significant, as shown in Figure 12. In this marked area either the maximum surface area, the breakup initiation time or the drag coefficient of the representative chain droplet differs more than 5% from those of an isolated droplet at the same conditions. As it is observed from the figure, the distance between the droplets is important when L/D_0 is less than 9 (or higher for low *We*). This indicates that most of the analytical models used for isolated droplets, when applied to droplet chains, are valid for L/D_o and *We* numbers higher than 9 and 20, correspondingly.

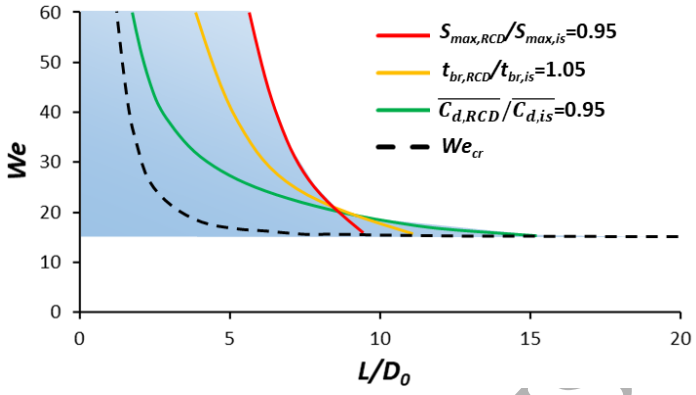

Figure 12. Area of influence of the distance between the droplets depicted in the L/D_0-*We* map along with the iso-lines of $S_{max,RCD}/S_{max,is}$, $t_{br,RCD}/t_{br,is}$, $\overline{C_{d,RCD}}/\overline{C_{d,is}}$ and the critical *We*.

Finally, the proposed correlations for the prediction of the critical *We* number, maximum droplet surface area, breakup initiation time, drag coefficient and average dimensionless deformation rate are summarized in Table 2, both for the representative chain and the isolated droplets (Appendix B). The equation for the prediction of the S_{max}/S_0 of the RCD shows a mean absolute error equal to 6.6% compared to the CFD simulations, that of the t_{br} equal to 3.7%, while that of the C_d equal to 6.8%. Sensitivity analysis regarding the proposed coefficients showed that when the coefficient c_1 (see equation (3)) is increased by 10% the mean absolute error compared to the results of the simulations becomes equal to 7.3% for the S_{max}, equal to 3.5% for the t_{br} and equal to 6.9% for the C_d. For a 10% increase in the coefficient c_2 the errors are calculated as 7.6% (S_{max}), 3.8% (t_{br}) and 8.1% (C_d), while for the c_3 they are equal to 6.4% (S_{max}), 3.5% (t_{br}) and 7% (C_d). It should be mentioned that in actual sprays several different droplet sizes are present and much more complicated phenomena would appear, something that is not considered in the present work.

Table 2. Summary of proposed correlations.

	Isolated droplet	Representative chain droplet	Correction factor
We_{cr}	[63]	$We_{cr,RCD} = We_{cr,is} \cdot CF_{We_{cr}}$	$CF_{We_{cr}} = 1 + 5.5 \cdot \left(\frac{L}{D_0}\right)^{-2.2}$
$\frac{S_{max}}{S_0}$	[50]	$\frac{S_{max,RCD}}{S_0} = \frac{S_{max,is}}{S_0} \cdot CF_{S_{max}}$	$CF_{S_{max}} = 1 - e^{-0.21 \cdot We^{0.35} \cdot (\frac{L}{D_0} - 1)^{0.79}}$
t_{br}	[51, 63, 69, 76]	$t_{br,RCD} = t_{br,is} \cdot CF_{t_{br}}$	$CF_{t_{br}} = 1 + e^{-0.1 \cdot We^{0.64} \cdot (\frac{L}{D_0} - 1)^{0.71}}$
C_d	$\overline{C_{d,is}} = 4 \cdot We^{-0.41}$	$\overline{C_{d,RCD}} = \overline{C_{d,is}} \cdot CF_{C_d}$	$CF_{C_d} = 1 - e^{-0.038 \cdot We^{1.1} \cdot (\frac{L}{D_0} - 1)^{0.53}}$
B	$B_{is} = 1 + 0.016 \cdot We^{1.5}$	$B_{RCD} = B_{is} \cdot CF_B$	$CF_B = 1 - e^{-1.2 \cdot We^{-0.21} \cdot (\frac{L}{D_0} - 1)^{0.88}}$

4 Conclusions

In the present study, the aerodynamic breakup of four Diesel droplets arranged in tandem formation was investigated numerically. The examined ambient conditions correspond to those of Diesel engines, while the *We* numbers range from 15 up to 64 and the non-dimensional distances between the droplets (L/D_0) from 1.25 up to 20.

The examination of the temporal evolution of droplet shapes revealed that the leading droplet has a similar shape and breakup mode with that of an isolated one at the same conditions, while the rest of the droplets are influenced by the presence of their upstream droplet, especially for small L/D_0. When the distance is small enough (L/D_0<5 for *We*=40) the shapes of the trailing droplets deviate from that of the isolated one, as they become more deformed in the streamwise direction, while also experiencing a new breakup mode termed as "shuttlecock", characterized by a stretching of the droplet at its periphery.

The results of the simulations revealed that the droplet surface area and drag coefficient of the third droplet of the row (representative chain droplet) are lower than those of the isolated one (in agreement with previous studies), while the breakup initiation time and the critical *We* number are higher. Overall, the effect of droplet distance is significant for L/D_0<9 (or higher for lower *We*) as either the maximum surface area, the breakup time or the drag coefficient of the representative chain droplet differs more than 5% from the corresponding values of the isolated droplet. Correlations were provided based on the simulations for the prediction of the aforementioned quantities of the representative chain droplet as functions of the corresponding quantity of an isolated droplet, which is a function of *We*, and of a correction factor that accounts for the interaction between the droplets, which is a function of *We* and L/D_0. Finally, the proposed correlations for the drag coefficient can be used in a simplified 0-D model, similar to those utilized in Lagrangian numerical codes, to predict more accurately the temporal evolution of droplet velocity of a representative chain droplet. The results of the 0-D model are compared with those of the simulations and a very good agreement is observed for droplet distance L/D_0 equal to 2 and intermediate to high *We* numbers (40-60), while a deviation starts appearing for larger droplet distances and high *We* (=60). It should be noted, however, that the linear approximation of droplet frontal area as a function of time, used in the present study, can be further improved by utilizing a more accurate model for the prediction of droplet deformation such the TAB, DDB or Clark's [77].

Acknowledgements

Financial support from the MSCA-ITN-ETN of the European Union's H2020 programme, under REA grant agreement n. 675676 is acknowledged.

Appendix A. Difference between the RCD of the current work with that of a seven-droplet chain

In order to estimate the difference between the RCD considered in this work with that of a seven-droplet chain, which is more representative of an infinite array of droplets, a simulation is performed with seven droplets at *We*=40 and L/D_0=2. Figure 13 depicts the shapes of the droplets at the time instance of t/t_{sh}=2.1, which corresponds to the time of breakup of the leading droplet. It is evident that the shapes of the droplets 3 to 6 are nearly identical. Moreover, the values of the drag

coefficient and maximum surface area of the droplets 4 and 5, which can be considered as representative in the seven-droplet chain, are very close and higher than those of the RCD up to 13.8% and 12.7%, respectively. Nevertheless, these differences are expected to decrease at higher *We* numbers and larger L/D_0. The simulation of four droplets is chosen in the current study instead of seven, because it is more suitable for parametric studies, since the computational cost for the simulation of seven droplets is increased by approximately 75% compared to that of four.

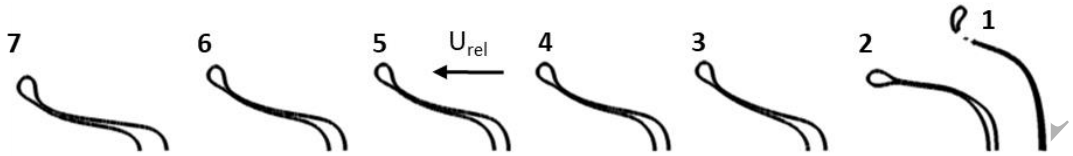

Figure 13. Droplet shapes at the time instance of t/t_{sh}=2.1 from the simulation of a chain of seven droplets arranged in tandem. *We*=40 and L/D_0=2.

Appendix B. Isolated droplet correlations

In [50] they proposed correlations for the prediction of the liquid surface area of an isolated droplet as function of *We*, and the reader is referred to that work for more details. For the prediction of the breakup initiation time the works of [51, 63, 69, 76] provide correlations that estimate it as function of the non-dimensional numbers (*We, Oh, Re, ε*). Regarding the critical *We* number this can be estimated as function of the non-dimensional numbers (*Oh*, *Re*, *ε*) using the equation proposed in [63]. Finally, the drag coefficient of an isolated droplet can be estimated as function of the *We* number using equation (9), similar to [66]. In the current simulations the *Re* number is a unilateral function of *We* (for a single *We* there is only one existing *Re*) so equation (9) can be written also as function of *Re*.

$$\overline{C_{d,ts}} = c_1 \cdot We^{-c2} \tag{9}$$

with c_1=4 and c_2=0.41 (mean absolute error equal to 8.6% compared to the simulations).

In Figure 14 the drag coefficient is presented as function of the *Re* number for the solid disk [78], solid sphere [78] as well as for deforming droplets calculated by the CFD simulations and the correlation (9). The predicted drag coefficients lie within the one of solid sphere (initial droplet shape) and the one of solid disk (deformed droplet shape) for the majority of the examined cases. In addition, both decrease with the *Re* number in agreement with that of solid sphere.

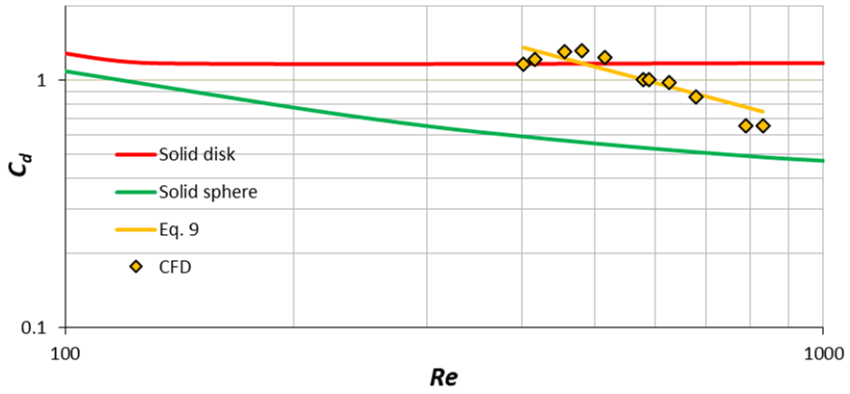

Figure 14. Drag coefficient as function of *Re* number for solid sphere, solid disk and for deforming droplets calculated by the CFD simulations and the correlation (9).

Similar to the method presented in section 3.5, equation (8) can be utilized to predict the temporal evolution of droplet velocity, where the C_d is given by equation (9) and the average dimensionless deformation rate by $B = c_1 \cdot We^{c_2}$ (with c_1=0.016, c_2=1.5 and mean absolute error equal to 9.9%). The predictions of equation (8) for three *We* numbers (15, 30 and 60) are presented in Figure 15 along with the results of the simulations for the same *We* numbers. For the low and intermediate *We* numbers of 15 and 30 there is a quite good agreement between the simulations and the correlation, while a deviation is observed for the higher *We* number of 60. This is attributed to the abrupt decline of droplet velocity, which is not easily captured by equation (8).

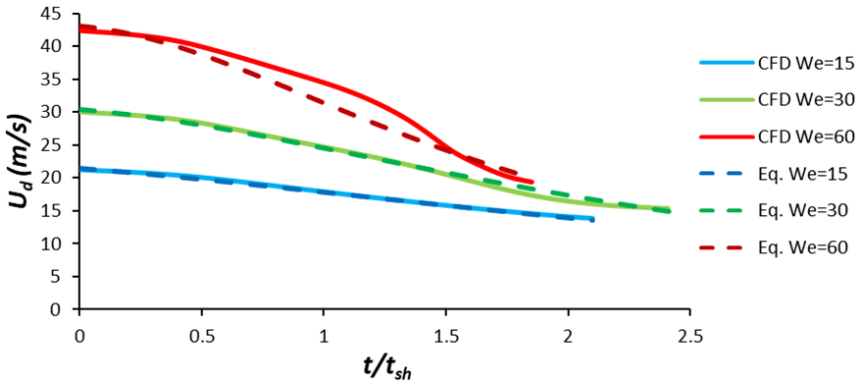

Figure 15. Temporal evolution of droplet velocity for three *We* numbers (15, 30 and 60) as predicted by the CFD simulations and correlation (8).

Appendix C. Quantitative comparison between droplets 1, 2, 3 and 4, and selection of the RCD

Figure 16 presents the temporal evolution of the deformation in both axes (cross-stream and streamwise) as well as the velocity for each of the four droplets of Figure 3 (*We*=40 and L/D_0=2). The droplets no. 2, 3 and 4 show similar evolution of deformation in both axes, while the droplet no.1 experiences larger cross-stream deformation and lower streamwise, due to the absence of an upstream droplet, as already discussed in section 3.1. Moreover, the droplet no.1 decelerates faster than the trailing ones due to higher drag, while the droplet no.2 decelerates slower due to lower

drag, since it is influenced by the wake of the 1st droplet, which has the largest cross-stream deformation. For the same reason its shape is also different from those of the 3rd and 4th droplets as seen in Figure 3. For these reasons the 2nd droplet cannot be considered as RCD. On the other hand, the droplets no. 3 and 4 show similar behaviour, but the droplet no.3 has a trailing droplet, which is more representative of an RCD, therefore justifying its selection as RCD.

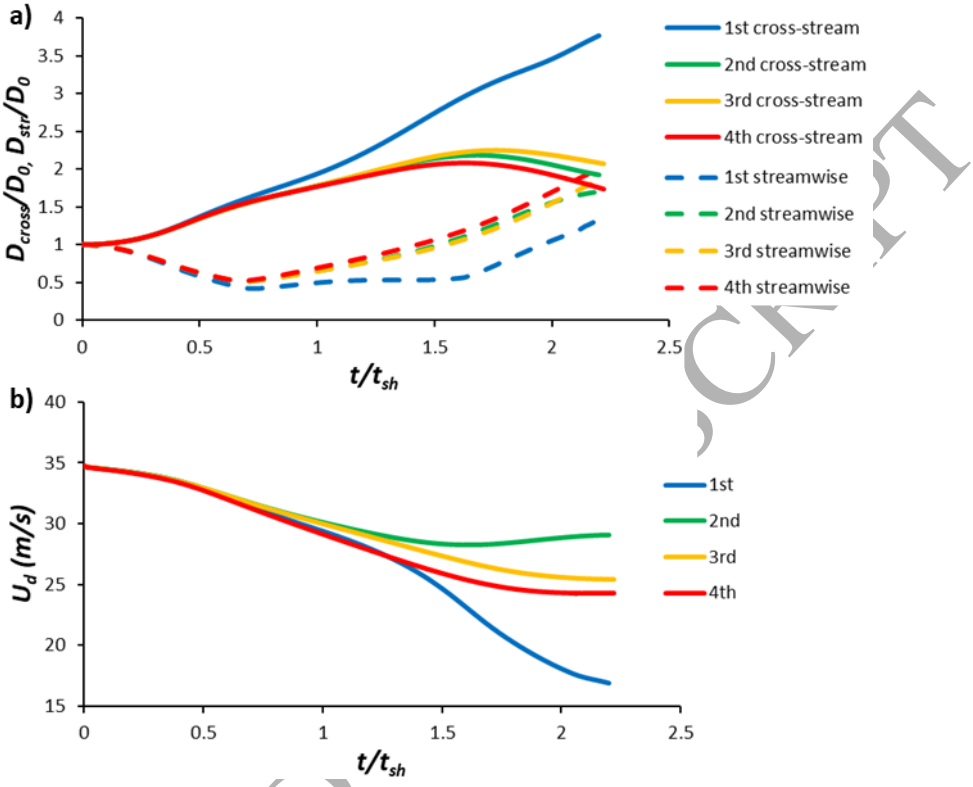

Figure 16. Temporal evolution of the a) deformation in both axes and b) velocity for each of the four droplets for a case with *We*=40 and L/D_0=2.

Appendix D. Drag coefficient with the inclusion of frontal area

Another way to calculate the drag coefficient is by including the effect of frontal area into it. In this approach, equation (10) is utilized to predict the droplet velocity as function of time (instead of equation (8)). Although this method is not as accurate as the one described in section 3.5, the latter is easier to use in macroscopic spray CFD models as it does not require tracking of the residence time of each particle in order to predict its temporal evolution of droplet velocity (by solving equation (10) numerically). In addition, this method can be used also for droplets experiencing solely deformation as it does not utilize equation (6) for the prediction of droplet frontal area, which is only valid for droplets experiencing breakup.

$$U_d(t^*) = \frac{U_{d,0}}{\overline{C_d} \cdot \frac{3}{4\sqrt{\varepsilon}} \cdot t^* + 1} \tag{10}$$

The ratio $\overline{C_{d,RCD}}/\overline{C_{d,ls}}$ is presented in Figure 17 as calculated by the simulations (scatter) and equation (3) (iso-lines) (with c_1=0.16, c_2=0.41, c_3=0.82 and mean absolute error equal to 4.8%). The

ratio reaches values as low as 0.24, compared to the value of 0.75 predicted by the method of section 3.5, while also being a weak function of *We* instead of a strong one as in section 3.5.

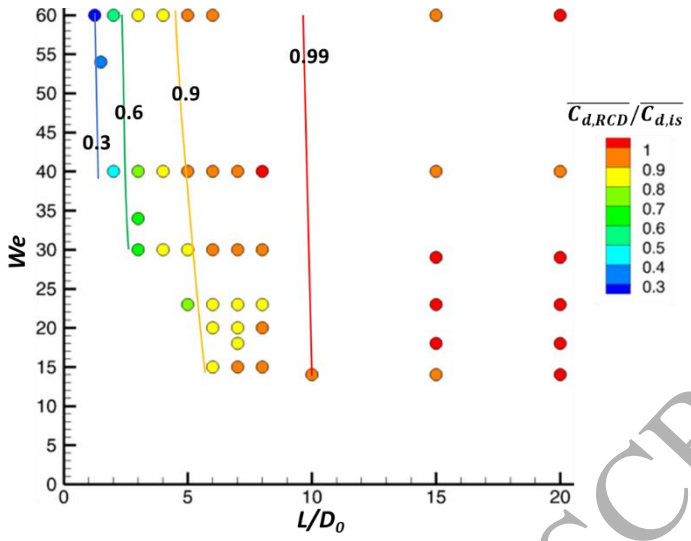

Figure 17. Ratio $\overline{C_{d,RCD}}/\overline{C_{d,is}}$ as function of *We* and L/D_0 (scatter: CFD, lines: equation (3)).

Finally, the temporal evolution of droplet velocity is given in Figure 18 for three *We* numbers (low, intermediate and high) both for an isolated droplet and a representative chain droplet with L/D_0=2, as predicted by equation (10) ($\overline{C_d}$ found from the equations (3) and (9)) and the CFD simulations. It is observed that similar to section 3.5, the agreement is good for the representative chain droplet, while for the isolated droplet a deviation is observed for the high *We* number. In addition, the prediction of droplet velocity using the equation shows opposite curvature compared to the simulations for both cases, owing to the exclusion of droplet frontal area.

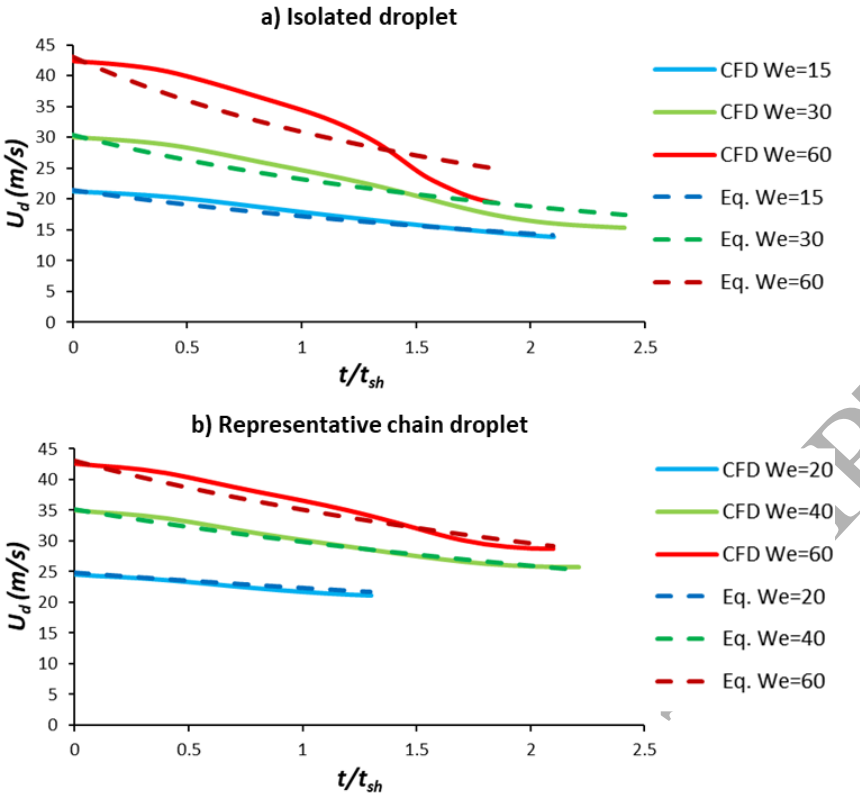

Figure 18. Temporal evolution of droplet velocity for three *We* numbers as predicted by the CFD simulations and the correlation (10) for a) an isolated droplet and b) a representative chain droplet with L/D_0=2.

References

[1] Ashgriz, N., 2011, Handbook of atomization and sprays: theory and applications, Springer Science & Business Media.
[2] Guildenbecher, D. R., López-Rivera, C., and Sojka, P. E., 2009, "Secondary atomization," Experiments in Fluids, 46(3), pp. 371-402.
[3] Nicholls, J. A., and Ranger, A. A., 1969, "Aerodynamic shattering of liquid drops," AIAA Journal, 7(2), pp. 285-290.
[4] Wadhwa, A. R., Magi, V., and Abraham, J., 2007, "Transient deformation and drag of decelerating drops in axisymmetric flows," Physics of Fluids (1994-present), 19(11), p. 113301.
[5] Lissaman, P., and Shollenberger, C. A., 1970, "Formation flight of birds," Science, 168(3934), pp. 1003-1005.
[6] Badgerow, J. P., and Hainsworth, F. R., 1981, "Energy savings through formation flight? A re-examination of the vee formation," Journal of Theoretical Biology, 93(1), pp. 41-52.
[7] Hummel, D., 1983, "Aerodynamic aspects of formation flight in birds," Journal of Theoretical Biology, 104(3), pp. 321-347.
[8] Hummel, D., 1995, "Formation flight as an energy-saving mechanism," Israel Journal of Zoology, 41(3), pp. 261-278.
[9] Nathan, A., and Barbosa, V. C., 2008, "V-like formations in flocks of artificial birds," Artificial life, 14(2), pp. 179-188.
[10] Bajec, I. L., and Heppner, F. H., 2009, "Organized flight in birds," Animal Behaviour, 78(4), pp. 777-789.
[11] Sewatkar, C., Sharma, A., and Agrawal, A., 2010, "A first attempt to numerically compute forces on birds in V formation," Artificial life, 16(3), pp. 245-258.
[12] Jian, D., and SHAO, X.-m., 2006, "Hydrodynamics in a diamond-shaped fish school," Journal of Hydrodynamics, Ser. B, 18(3), pp. 438-442.
[13] Wu, C., and Wang, L., 2009, "Numerical simulations of self-propelled swimming of 3D bionic fish school," Science in China Series E: Technological Sciences, 52(3), pp. 658-669.
[14] Hemelrijk, C., Reid, D., Hildenbrandt, H., and Padding, J., 2015, "The increased efficiency of fish swimming in a school," Fish and Fisheries, 16(3), pp. 511-521.
[15] Becker, A. D., Masoud, H., Newbolt, J. W., Shelley, M., and Ristroph, L., 2015, "Hydrodynamic schooling of flapping swimmers," Nature communications, 6, p. 8514.
[16] Daghooghi, M., and Borazjani, I., 2015, "The hydrodynamic advantages of synchronized swimming in a rectangular pattern," Bioinspiration & biomimetics, 10(5), p. 056018.
[17] Chen, S.-Y., Fei, Y.-H. J., Chen, Y.-C., Chi, K.-J., and Yang, J.-T., 2016, "The swimming patterns and energy-saving mechanism revealed from three fish in a school," Ocean Engineering, 122, pp. 22-31.
[18] Khalid, M. S. U., Akhtar, I., and Dong, H., 2016, "Hydrodynamics of a tandem fish school with asynchronous undulation of individuals," Journal of Fluids and Structures, 66, pp. 19-35.
[19] Maertens, A. P., Gao, A., and Triantafyllou, M. S., 2017, "Optimal undulatory swimming for a single fish-like body and for a pair of interacting swimmers," Journal of Fluid Mechanics, 813, pp. 301-345.
[20] Park, S. G., and Sung, H. J., 2018, "Hydrodynamics of flexible fins propelled in tandem, diagonal, triangular and diamond configurations," Journal of Fluid Mechanics, 840, pp. 154-189.
[21] Liu, D., Anders, K., and Frohn, A., 1988, "Drag coefficients of single droplets moving in an infinite droplet chain on the axis of a tube," International Journal of Multiphase Flow, 14(2), pp. 217-232.
[22] Mulholland, J., Srivastava, R., and Wendt, J., 1988, "Influence of droplet spacing on drag coefficient in nonevaporating, monodisperse streams," AIAA Journal, 26(10), pp. 1231-1237.
[23] Temkin, S., and Ecker, G., 1989, "Droplet pair interactions in a shock-wave flow field," Journal of Fluid Mechanics, 202, pp. 467-497.
[24] Poo, J., and Ashgriz, N., 1991, "Variation of drag coefficients in an interacting drop stream," Experiments in Fluids, 11(1), pp. 1-8.
[25] Nguyen, Q., and Dunn-Rankin, D., 1992, "Experiments examining drag in linear droplet packets," Experiments in Fluids, 12(3), pp. 157-165.
[26] Connon, C., and Dunn-Rankin, D., 1996, "Flow behavior near an infinite droplet stream," Experiments in Fluids, 21(2), pp. 80-86.
[27] Holländer, W., and Zaripov, S., 2005, "Hydrodynamically interacting droplets at small Reynolds numbers," International Journal of Multiphase Flow, 31(1), pp. 53-68.
[28] Kim, I., Elghobashi, S., and Sirignano, W., 1991, "Three-dimensional droplet interactions in dense sprays," 29th Aerospace Sciences Meeting, American Institute of Aeronautics and Astronautics.
[29] Kim, I., Elghobashi, S., and Sirignano, W., "Three-dimensional flow computation for two interacting, moving droplets," Proc. AIAA Materials Specialist Conference-Coating Technology for Aerospace Systems.
[30] Kim, I., Elghobashi, S., and Sirignano, W. A., 1993, "Three-dimensional flow over two spheres placed side by side," Journal of Fluid Mechanics, 246, pp. 465-488.
[31] Prahl, L., Revstedt, J., and Fuchs, L., "Interaction among droplets in a uniform flow at intermediate Reynolds numbers," Proc. 44th AIAA Aerospace Sciences Meeting and Exhibit, Reno, Nevada, USA, January, pp. 9-12.
[32] Quan, S., "Dynamics of Droplets Impulsively Accelerated by Gaseous Flow:A Numerical Investigation," Proc. ICLASS 2009, 11th Triennial International Annual Conference on Liquid Atomization and Spray Systems.
[33] Quan, S., Lou, J., and Stone, H. A., 2011, "Interactions between two deformable droplets in tandem subjected to impulsive acceleration by surrounding flows," Journal of Fluid Mechanics, 684, pp. 384-406.
[34] Magi, V., and Abraham, J., 2012, "Drop Interactions in Transient Flows with Applications to Liquid Sprays."

[35] Hirt, C. W., and Nichols, B. D., 1981, "Volume of fluid (VOF) method for the dynamics of free boundaries," Journal of Computational Physics, 39(1), pp. 201-225.
[36] Lafaurie, B., Nardone, C., Scardovelli, R., Zaleski, S., and Zanetti, G., 1994, "Modelling Merging and Fragmentation in Multiphase Flows with SURFER," Journal of Computational Physics, 113(1), pp. 134-147.
[37] "ANSYS®FLUENT, 2014, Release 16.0."
[38] Versteeg, H. K., and Malalasekera, W., 2007, An introduction to computational fluid dynamics: the finite volume method, Pearson Education.
[39] Issa, R. I., 1986, "Solution of the implicitly discretised fluid flow equations by operator-splitting," Journal of Computational Physics, 62(1), pp. 40-65.
[40] "ANSYS®FLUENT Theory Guide, 2014, Release 16.0."
[41] Barth, T., and Jespersen, D., "The design and application of upwind schemes on unstructured meshes," Proc. 27th Aerospace sciences meeting, p. 366.
[42] Malgarinos, I., Nikolopoulos, N., and Gavaises, M., 2015, "Coupling a local adaptive grid refinement technique with an interface sharpening scheme for the simulation of two-phase flow and free-surface flows using VOF methodology," Journal of Computational Physics, 300, pp. 732-753.
[43] Strotos, G., Malgarinos, I., Nikolopoulos, N., and Gavaises, M., 2016, "Numerical investigation of aerodynamic droplet breakup in a high temperature gas environment," Fuel, 181, pp. 450-462.
[44] Malgarinos, I., Nikolopoulos, N., Marengo, M., Antonini, C., and Gavaises, M., 2014, "VOF simulations of the contact angle dynamics during the drop spreading: Standard models and a new wetting force model," Advances in Colloid and Interface Science, 212, pp. 1-20.
[45] Malgarinos, I., Nikolopoulos, N., and Gavaises, M., 2016, "A numerical study on droplet-particle collision dynamics," International Journal of Heat and Fluid Flow, 61, Part B, pp. 499-509.
[46] Malgarinos, I., Nikolopoulos, N., and Gavaises, M., 2017, "Numerical investigation of heavy fuel droplet-particle collisions in the injection zone of a Fluid Catalytic Cracking reactor, Part I: Numerical model and 2D simulations," Fuel Processing Technology, 156, pp. 317-330.
[47] Malgarinos, I., Nikolopoulos, N., and Gavaises, M., 2017, "Numerical investigation of heavy fuel droplet-particle collisions in the injection zone of a Fluid Catalytic Cracking reactor, part II: 3D simulations," Fuel Processing Technology, 156, pp. 43-53.
[48] G. Strotos, I. M., N. Nikolopoulos, K. Papadopoulos, A. Theodorakakos, M.Gavaises, 2015, "Performance of VOF methodology in predicting the deformation and breakup of impulsively accelerated droplets," ICLASS 2015, 13th Triennial International Conference on Liquid Atomization and Spray Systems, August 23-27Tainan, Taiwan.
[49] Strotos, G., Malgarinos, I., Nikolopoulos, N., and Gavaises, M., 2016, "Predicting droplet deformation and breakup for moderate Weber numbers," International Journal of Multiphase Flow, 85, pp. 96-109.
[50] Strotos, G., Malgarinos, I., Nikolopoulos, N., and Gavaises, M., 2016, "Aerodynamic breakup of an n-decane droplet in a high temperature gas environment," Fuel, 185, pp. 370-380.
[51] Stefanitsis, D., Malgarinos, I., Strotos, G., Nikolopoulos, N., Kakaras, E., and Gavaises, M., 2017, "Numerical investigation of the aerodynamic breakup of Diesel and heavy fuel oil droplets," International Journal of Heat and Fluid Flow, 68, pp. 203-215.
[52] Stefanitsis, D., Malgarinos, I., Strotos, G., Nikolopoulos, N., Kakaras, E., and Gavaises, M., 2017, "Numerical investigation of the aerodynamic breakup of Diesel droplets under various gas pressures," 28th Conference on Liquid Atomization and Spray Systems (ILASS-Europe 2017)Valencia, Spain.
[53] Strotos, G., Malgarinos, I., Nikolopoulos, N., and Gavaises, M., 2016, "Predicting the evaporation rate of stationary droplets with the VOF methodology for a wide range of ambient temperature conditions," International Journal of Thermal Sciences, 109, pp. 253-262.
[54] Jain, M., Prakash, R. S., Tomar, G., and Ravikrishna, R. V., 2015, "Secondary breakup of a drop at moderate Weber numbers," Proceedings of the Royal Society A: Mathematical, Physical and Engineering Science, 471(2177).
[55] Jain, S. S., Tyagi, N., Prakash, R. S., Ravikrishna, R., and Tomar, G., 2018, "Secondary breakup of drops at moderate Weber numbers: Effect of Density ratio and Reynolds number," arXiv preprint arXiv:1803.02989.
[56] Liang, C., 2016, "Computational methods for the investigation of liquid drop phenomena in external gas flows."
[57] Kékesi, T., Amberg, G., and Prahl Wittberg, L., 2014, "Drop deformation and breakup," International Journal of Multiphase Flow, 66, pp. 1-10.
[58] Kékesi, T., Altimira, M., Amberg, G., and Prahl Wittberg, L., 2017, "Interaction between two deforming liquid drops in tandem and various off-axis arrangements subject to uniform flow."
[59] Lacaze, G., Misdariis, A., Ruiz, A., and Oefelein, J. C., 2015, "Analysis of high-pressure Diesel fuel injection processes using LES with real-fluid thermodynamics and transport," Proceedings of the Combustion Institute, 35(2), pp. 1603-1611.
[60] Sutherland, W., 1893, "LII. The viscosity of gases and molecular force," The London, Edinburgh, and Dublin Philosophical Magazine and Journal of Science, 36(223), pp. 507-531.
[61] Mueller, C. J., Cannella, W. J., Bays, J. T., Bruno, T. J., DeFabio, K., Dettman, H. D., Gieleciak, R. M., Huber, M. L., Kweon, C.-B., McConnell, S. S., Pitz, W. J., and Ratcliff, M. A., 2016, "Diesel Surrogate Fuels for Engine Testing and Chemical-Kinetic Modeling: Compositions and Properties," Energy & Fuels, 30(2), pp. 1445-1461.
[62] Yaws, C. L., and Gabbula, C., 2003, Yaws" Handbook of Thermodynamic and Physical Properties of Chemical Compounds, Knovel.

[63] Strotos, G., Malgarinos, I., Nikolopoulos, N., Gavaises, M., Nikas, K.-S., and Moustris, K., 2018, "Determination of the aerodynamic droplet breakup boundaries based on a total force approach," International Journal of Heat and Fluid Flow, 69, pp. 164-173.
[64] Loth, E., and Dorgan, A. J., 2009, "An equation of motion for particles of finite Reynolds number and size," Environmental fluid mechanics, 9(2), pp. 187-206.
[65] Quan, S., and Schmidt, D. P., 2006, "Direct numerical study of a liquid droplet impulsively accelerated by gaseous flow," Physics of Fluids (1994-present), 18(10), p. 102103.
[66] Khare P., V. Y., "Drag Coefficients of Deforming and Fragmenting Liquid Droplets," Proc. ILASS Americas, 25th Annual Conference on Liquid Atomization and Spray Systems.
[67] Yang, W., Jia, M., Sun, K., and Wang, T., 2016, "Influence of density ratio on the secondary atomization of liquid droplets under highly unstable conditions," Fuel, 174, pp. 25-35.
[68] Shao, C., Luo, K., and Fan, J., 2017, "Detailed numerical simulation of unsteady drag coefficient of deformable droplet," Chemical Engineering Journal, 308, pp. 619-631.
[69] Pilch, M., and Erdman, C. A., 1987, "Use of breakup time data and velocity history data to predict the maximum size of stable fragments for acceleration-induced breakup of a liquid drop," International Journal of Multiphase Flow, 13(6), pp. 741-757.
[70] Schmehl, R., 2002, "Advanced modeling of droplet deformation and breakup for CFD analysis of mixture preparation," Zaragoza, 9(11).
[71] Liu, A. B., Mather, D., and Reitz, R. D., 1993, "Modeling the effects of drop drag and breakup on fuel sprays," WISCONSIN UNIV-MADISON ENGINE RESEARCH CENTER.
[72] Bartz, F., Guildenbecher, D., Schmehl, R., Koch, R., Bauer, H., and Sojka, P., "Model comparison for single droplet fragmentation under varying accelerations," Proc. 24th European conference on liquid atomization and spray systems.
[73] O'Rourke, P. J., and Amsden, A. A., 1987, "The TAB method for numerical calculation of spray droplet breakup," No. 0148-7191, SAE Technical Paper.
[74] Ibrahim, E., Yang, H., and Przekwas, A., 1993, "Modeling of spray droplets deformation and breakup," Journal of Propulsion and Power, 9(4), pp. 651-654.
[75] Clark, M. M., 1988, "Drop breakup in a turbulent flow—I. Conceptual and modeling considerations," Chemical Engineering Science, 43(3), pp. 671-679.
[76] Gel'fand, B. E., Gubin, S. A., Kogarko, S. M., and Komar, S. P., 1973, "Singularities of the breakup of viscous liquid droplets in shock waves," Journal of engineering physics, 25(3), pp. 1140-1142.
[77] Lee, M. W., Park, J. J., Farid, M. M., and Yoon, S. S., 2012, "Comparison and correction of the drop breakup models for stochastic dilute spray flow," Applied Mathematical Modelling, 36(9), pp. 4512-4520.
[78] Clift, R., Grace, J. R., and Weber, M. E., 2005, Bubbles, drops, and particles, Courier Corporation.